

# Cloud motion vectors from a network of ground sensors in a solar power plant

J.L. Bosch\*, J. Kleissl

*Department of Mechanical and Aerospace Engineering  
Center for Renewable Resources and Integration  
University of California, San Diego  
La Jolla, California 92093-0411*

---

## Abstract

Clouds are the dominant source of PV power output variability and their velocity is a principal input to most short-term forecast models. A new method for deriving cloud speed from data collected at a triplet of sensors at arbitrary positions is presented; cloud speed and the angle of the cloud front are determined from the time delays in two cloud front arrivals at the sensors. Five reference cells at the 48 MW PV plant at Henderson (NV), were used to provide two different triplets of sensors. Over a year of operation cloud speeds from 3 to 35 m s<sup>-1</sup> were obtained. Cloud speeds are validated using cross-correlation of power output from 96 inverters at the plant. Overall bias errors were less than 1% and the overall annual RMSE was 20.9%, but results varied with season.

*Keywords:* solar forecasting, solar radiation, cloud motion detection

---

## 1. Introduction

Solar photovoltaic (PV) power output variability caused by clouds is a major barrier to expansion of solar power (e.g. [Pelland et al. \(2011\)](#)). Cloud velocity is a principal input to most short-term forecast ([Chow et al. \(2011\)](#); [Perez et al. \(2010\)](#); [Yang et al. \(2013\)](#)) and variability models ([Arias-Castro et al. \(2013\)](#); [Hoff and Perez \(2010\)](#); [Lave and Kleissl \(2013\)](#)). In simple terms for a cloud passage, the ramp magnitude depends on the cloud optical depth; in addition the ramp rate is a function of how long it takes for a cloud to cover the plant, i.e. the cloud speed.

Cloud Motion Vectors (CMVs) have traditionally been obtained from satellite imagery ([Hammer et al. \(1999\)](#); [Leese et al. \(1971\)](#); [Lorenz et al. \(2004\)](#)) by tracking a feature in successive images. A statistical method based on conditional probabilities for the motion vector field ([Hammer et al. \(1999\)](#)) predicted

---

\*Corresponding Author. Tel.: (858)5348087; fax: (858)5347599.  
E-mail Address: [jlbosch@ucsd.edu](mailto:jlbosch@ucsd.edu)

solar radiation up to 2 hours ahead. [Lorenz et al. \(2004\)](#) used a similar method to obtain solar radiation forecast up to 6 hours ahead. For longer forecast time horizons, non-linearities in atmospheric motion and cloud formation and evaporation cause Numerical Weather Prediction (NWP) models to outperform satellite-based CMV forecasts ([Perez et al. \(2010\)](#)).

However, not only are satellite data complex to acquire and process, but infrequent data update (every 15 to 30 min in the case of the GOES-W satellite which covers the area studied in this paper) and data transfer delays also may not allow detection of mesoscale convective clouds in a timely manner. Consequently, local ground measurements of cloud speed are advantageous for short-term solar variability and solar forecasting.

The main goal in this study is to estimate cloud speed without additional instrumentation using time delays in cloud arrival times detected using triplets of reference cells and inverter output of a solar power plant. The principal assumption is that the cloud edge shadow can be considered linear and cloud speed constant as the cloud passes over the triplet. Previous work by [Bosch et al. \(2013\)](#) covered a special case of sensors arranged orthogonally, equidistant, and in close proximity. CMV detection required fast data sampling rates and the validation was limited to four days. The conditions on the sensors set up in the present paper are less restrictive and results are validated with a year of data. Section 2 describes the data set, Section 3 presents the methods and quality control process utilized to derive CMVs from the data. The results obtained after applying these methods to a year of data are presented and discussed in Section 4.

## Nomenclature

$\alpha$	Angle between the cloud direction and the pair of sensors $oA$ [ $^\circ$ ].
$\alpha_0$	Angle between the West-East direction and the pair of sensors $oA$ [ $^\circ$ ].
$\beta$	Angle between the cloud edge and the pair of sensors $oA$ [ $^\circ$ ].
$\theta$	Angle between the pairs of sensors $oA$ and $oB$ [ $^\circ$ ].
<i>CCM</i>	Cross-Correlation Method.
<i>CMV</i>	Cloud Motion Vector.
<i>LCE</i>	Linear Cloud Edge.
<i>NWP</i>	Numerical Weather Prediction.
<i>MBE</i>	Mean Bias Error.
<i>PST</i>	Pacific Standard Time.
<i>RMSE</i>	Root Mean Squared Error.

$C_A$	Point of the cloud edge shadow that passes over sensor $A$ .
$C_B$	Point of the cloud edge shadow that passes over sensor $B$ .
$\hat{\mathbf{c}}$	Unitary vector in the direction of the cloud edge.
$D$	Distance between sensors $S_a$ and $S_b$ .
$d_A$	Distance between sensors $o$ and $A$ in a given triplet [m].
$d_B$	Distance between sensors $o$ and $B$ in a given triplet [m].
$I_a, I_b$	Global Irradiances received at sensors $S_a$ and $S_b$ [ $\text{W m}^{-2}$ ].
$I_{POA}$	Plane of Array Irradiance [ $\text{W m}^{-2}$ ].
$\mathbf{r}$	Position vector (e.g. $\mathbf{r}_o$ is the position vector of sensor $o$ ) [m].
$t_A$	Time needed for the cloud shadow to move from $C_A$ to sensor $A$ [s].
$t_B$	Time needed for the cloud shadow to move from $C_B$ to sensor $B$ [s].
$t_{ab}$	Time lag obtained from the maximum cross correlation of signals $I_a$ and $I_b$ .
$\mathbf{v}$	Cloud motion vector [ $\text{m s}^{-1}$ ].
$v$	Magnitude of the cloud motion vector, or cloud speed [ $\text{m s}^{-1}$ ].
$v_m$	Cloud speed determined using CCM [ $\text{m s}^{-1}$ ].
$v_l$	Cloud speed determined using LCE [ $\text{m s}^{-1}$ ].

## 2. Data

Plane-of-Array irradiance  $I_{POA}$  was measured using 5 reference cells at the Sempra US Gas & Power Copper Mountain Solar 1 48 MW PV Plant (Latitude  $35.78^\circ$ ; Longitude  $-115.00^\circ$ ) with a sampling rate of 1 s. Copper Mountain Solar 1 consists of nearly one million thin-film Cd-Te PV panels model FS-272, FS-275 and FS-277 spread across more than  $1.8 \text{ km}^2$  (First Solar, 2011). The reference cells are tilted towards south and the selected ones can be combined in two different triplets, as shown in Fig. 1. Other reference cell triplets exist, but they were not selected due to their larger spacing (520 m or more). Table 1 shows the distances and angles of the selected triplets.

In addition, power output from the 96 inverters located at the plant were used to validate the cloud speed results obtained from the reference cell triplets. This second set of data was also acquired at 1 s temporal resolution and has a typical uncertainty of 1-2%. Other specifications and model names are not provided due to confidentiality of the data.

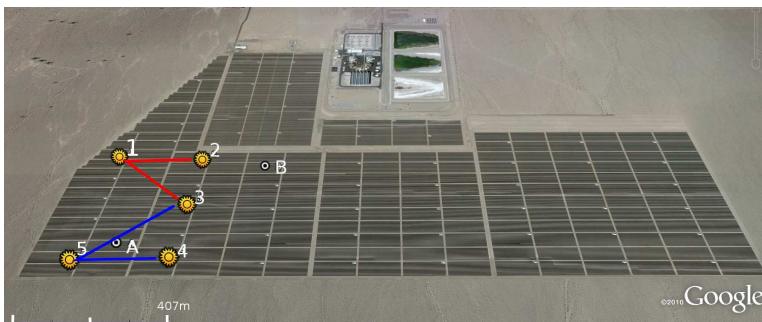


Figure 1: Power plant layout showing the selected reference cells. White boxes near the 'aisles' of the panel blocks correspond to inverter locations (Google Earth, 2013).

Table 1: Description of the two triplets. Consult Fig. 1 for sensor numbers and variables names are defined in Fig. 2.

Triplet	T1	T2
Sensor $o$	1	5
Sensor A	2	4
Sensor B	3	3
$\alpha_0$ [°]	-3.2	+1.5
$\theta$ [°]	-36.0	+36.7
$d_A$ [m]	284	283
$d_B$ [m]	365	360

### 3. Methods

#### 3.1. Linear Cloud Edge (LCE)

Consider a triplet of sensors  $o$ ,  $A$  and  $B$ , in an arbitrary arrangement (Fig. 2). For simplicity, we will consider the sensor  $o$  as the origin of the coordinate system, and the  $x$  axis to be aligned with the  $\overline{oA}$  direction. A sample cloud edge passing through the array is shown in Fig. 3 using the defined coordinate system.

We define the time needed for the cloud to move from  $C_A$  to  $A$ , ( $t_A$ ) and from  $C_B$  to  $B$ , ( $t_B$ ). The cloud motion direction is given by either the lines  $\overline{BC_B}$ ,  $\overline{C_AA}$  or the motion vector  $\mathbf{v}$ . Equations 1-13 show the steps to calculate the CMV.

The main vectors in Fig. 3 can be expressed as:

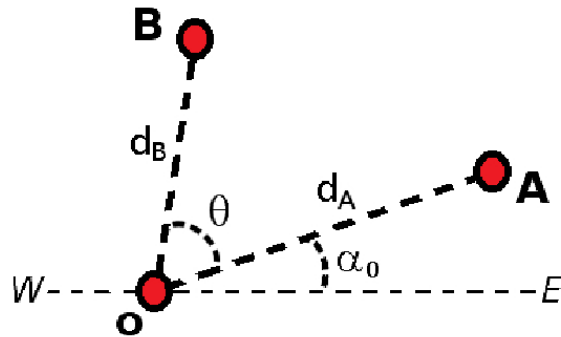


Figure 2: Arbitrary triplet of sensors where  $\alpha_0$  is the angle between the West-East direction and the line  $\overline{oA}$ , and  $\theta$  is the angle between the two pairs of sensors  $\overline{oA}$  and  $\overline{oB}$ . The distances from sensor  $o$  to sensors  $A$  and  $B$  are given by  $d_A$  and  $d_B$  respectively.

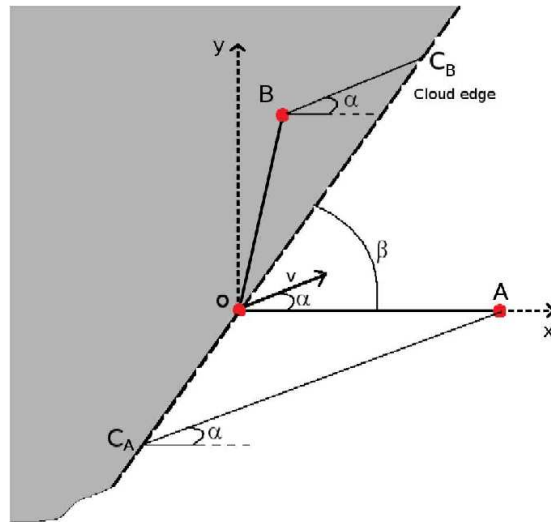


Figure 3: Schematic of a linear cloud edge passing a sensor triplet.  $\beta$  is the angle between the cloud edge and the  $x$  axis, and  $\alpha$  is the angle between the CMV  $\mathbf{v}$  and the  $x$  axis.  $C_A$  and  $C_B$  are the cloud edge points that pass over sensors  $A$  and  $B$ .

$$\begin{aligned}
\mathbf{v} &= (v \cos \alpha, v \sin \alpha) \\
\mathbf{r}_o &= (0, 0) \\
\mathbf{r}_A &= (d_A, 0) \\
\mathbf{r}_B &= (d_B \cos \theta, d_B \sin \theta) \\
\mathbf{r}_{C_A} &= \frac{oC_A}{\hat{\mathbf{c}}} \\
\mathbf{r}_{C_B} &= \frac{oC_B}{\hat{\mathbf{c}}} \\
\hat{\mathbf{c}} &= (\cos \beta, \sin \beta)
\end{aligned} \tag{1}$$

Where  $\hat{\mathbf{c}}$  is an unitary vector in the direction of the cloud edge. Basic kinematic equations can be used to reach the analytic expressions for  $t_A$  and  $t_B$

$$\begin{aligned}
\mathbf{r}_A &= \mathbf{r}_{C_A} + t_A \mathbf{v} \\
\mathbf{r}_B &= \mathbf{r}_{C_B} + t_B \mathbf{v}
\end{aligned} \tag{2}$$

Applying the cross product with  $\hat{\mathbf{c}}$ :

$$t_A = \frac{\mathbf{r}_A \times \hat{\mathbf{c}}}{\mathbf{v} \times \hat{\mathbf{c}}} \tag{3}$$

$$t_B = \frac{\mathbf{r}_B \times \hat{\mathbf{c}}}{\mathbf{v} \times \hat{\mathbf{c}}} \tag{4}$$

In general, it can be deduced from Eqs. 3-4 that if a sensor pair is parallel to the cloud edge, the shadow will reach both sensors at the same time simplifying the problem. For example, if sensors  $o$  and  $B$  are parallel to the cloud edge, then  $t_B$  will be 0 and  $\beta$  will be equal to  $\theta$ . On the other hand, if the cloud motion vector is parallel to the cloud edge, the shadow will always be on the origin and never reach the other sensors.

Defining the vectors  $\mathbf{v}_A$  and  $\mathbf{v}_B$

$$\begin{aligned}
\mathbf{v}_A &= \mathbf{r}_A / t_A \\
\mathbf{v}_B &= \mathbf{r}_B / t_B,
\end{aligned} \tag{5}$$

Eq. 2 can be rewritten as:

$$\begin{aligned}
\mathbf{v}_A \times \hat{\mathbf{c}} &= \mathbf{v} \times \hat{\mathbf{c}} \\
\mathbf{v}_B \times \hat{\mathbf{c}} &= \mathbf{v} \times \hat{\mathbf{c}}.
\end{aligned} \tag{6}$$

### 3.1.1. Solving for the cloud edge angle $\beta$

Solving Eqs. 6 yields

$$\mathbf{v}_A \times \hat{\mathbf{c}} = \mathbf{v}_B \times \hat{\mathbf{c}}, \tag{7}$$

where  $\beta$  can be solved after substitution of the values listed in Eq. 1.

$$\frac{d_A}{t_A} \sin \beta = \frac{d_B}{t_B} \sin(\beta - \theta) \tag{8}$$

$$\beta = \arctan \left[ \frac{-v_B \sin \theta}{v_A - v_B \cos \theta} \right]. \tag{9}$$

[It is worth noting that for  $\theta = \pi/2$ , Eq. 9 yields the equations derived in for an orthogonal triplet

$$\beta = \arctan \left[ -\frac{t_B d_A}{t_A d_B} \right] \quad (10)$$

And for equal distances  $d_A = d_B = D$ :

$$\beta = \arctan \left[ -\frac{t_B}{t_A} \right] \quad (11)$$

in Bosch et al. (2013)]. Equation 9 demonstrates that one triplet of unaligned sensors is enough to obtain  $\beta$ . However, the CMV cannot be obtained in this way. Also note that adding new sensors would not allow solving for the CMV for a single cloud passage because the left-hand side of Eq. 6 is independent of sensor location. The additional information needed to solve for the CMV must be obtained from a second cloud edge passage through the sensors, with the same  $v$  and  $\alpha$ , but with a different  $\beta$ .

### 3.1.2. Solving for the cloud motion vector

Finally, replacing  $\beta$  from Eq. 9 into Eq. 6, the system reduces to:

$$\frac{-v \sin \alpha}{v_A - v \cos \alpha} = \frac{-v_B \sin \theta}{v_A - v_B \cos \theta} \quad (12)$$

Since the time lags  $t_A$  and  $t_B$  (i.e.  $v_A$  and  $v_B$ ) can be obtained from the measurements and the sensor locations are known, we are left with two unknowns ( $\alpha$  and  $v$ ), and one equation (Eq. 12).

Assigning the indices 1 and 2 for the first and second cloud passage, respectively, leads to Eq. 13

$$\alpha = \arctan \left[ \frac{-d_B \sin \theta (t_{A1} - t_{A2})}{d_A (t_{B1} - t_{B2}) - d_B \cos \theta (t_{A1} - t_{A2})} \right] \quad (13)$$

Once  $\alpha$  is obtained from Eq. 13,  $v$  can be calculated using Eq. 12. The final step to obtain the cloud cardinal direction is to apply the  $\alpha_0$  rotation defined in Fig. 2 to the calculated  $\alpha$ .

Again, applying the restriction of orthogonality ( $\theta = \pi/2$ ) the equation is reduced to the one presented in Bosch et al. (2013).

$$\alpha = \arctan \left[ \frac{-d_B (t_{A1} - t_{A2})}{d_A (t_{B1} - t_{B2})} \right] \quad (14)$$

### 3.1.3. Obtaining time lags

Attempts to determine the time lags  $t_A$  and  $t_B$  from the cross-correlation method (Bosch et al. (2013)) or from the timing of the largest ramps (edge overpass) were unsuccessful. Rather  $t_A$  and  $t_B$  are determined from the timing of local maxima and minima of the measured  $I_{POA}$ . The maxima can occur when cloud enhancement causes an increase in  $I_{POA}$  just before or after a cloud

shades the sensors, while minima in  $I_{POA}$  occur near the cloud center. More often, maxima and minima occur during the shading event due to variability in intra-cloud opacity. Time lags between the maxima and minima observed at different sensor locations yield  $t_A$  and  $t_B$  for particular cloud events.

### 3.2. Data quality control

#### 3.2.1. Raw data

High data acquisition frequency can lead to noisy signals. Local maxima and minima could then be caused by noise rather than atmospheric effects leading to errors in both the cloud speed and direction. To avoid this and other erroneous maxima and minima detection, a preprocessing similar to that described in [Bosch et al. \(2013\)](#) is conducted. First, a 5-point (corresponding to 5 s) moving average is applied and global maxima over a moving window of 50 s are selected; from the remaining maxima, only those with 5 monotonous ascending values before the maxima and 5 monotonous descending values after the maxima are selected; groups of maxima from different sensors belonging to the same cloud are identified using a 150 s window.

The three different times for the simultaneous maxima yield the time lags  $t_A$  and  $t_B$  for each event, but two events are needed to obtain the CMV (see Eq. 13). If two events were too far separated in time, the assumption of constant CMVs may be violated. Consequently, two cloud events are required to occur within 15 min. The same process is repeated for the minima, producing another set of CMVs.

#### 3.2.2. Two-dimensional quality control

Even after the quality control for the selection of minima and maxima the resulting CMVs display considerable variability in cloud direction and especially cloud speed (Fig. 4a,b). To determine the final CMV, the most frequent CMV in the last hour is selected. While the mode is often not expressed in histograms of one variable, the most prevalent pair can be obtained from the density maximum in the 2-D distribution of CMVs. Each point in the scatter plot (Fig. 4c) represents a CMV, and the color scale indicates the number of points in the vicinity of each CMV (here the vicinity is defined as a five units ratio around the point). The final CMV is the point with the highest density using a moving window of one hour.

### 3.3. Cross-correlation method (CCM)

When the LCE method yielded a CMV, the cross-correlation method was applied at the same time to obtain an independent validation. The basic premise is that for a pair of sensors  $S_a$  and  $S_b$  aligned with the cloud motion, separated by a distance  $D$ , the irradiances  $I_a$  and  $I_b$  are highly correlated, but with a time lag  $t_{ab}$  (Fig. 5). Once the lag has been determined (e.g. by analyzing the signal cross correlation), cloud speed can be calculated as

$$v = D/t_{ab} \tag{15}$$

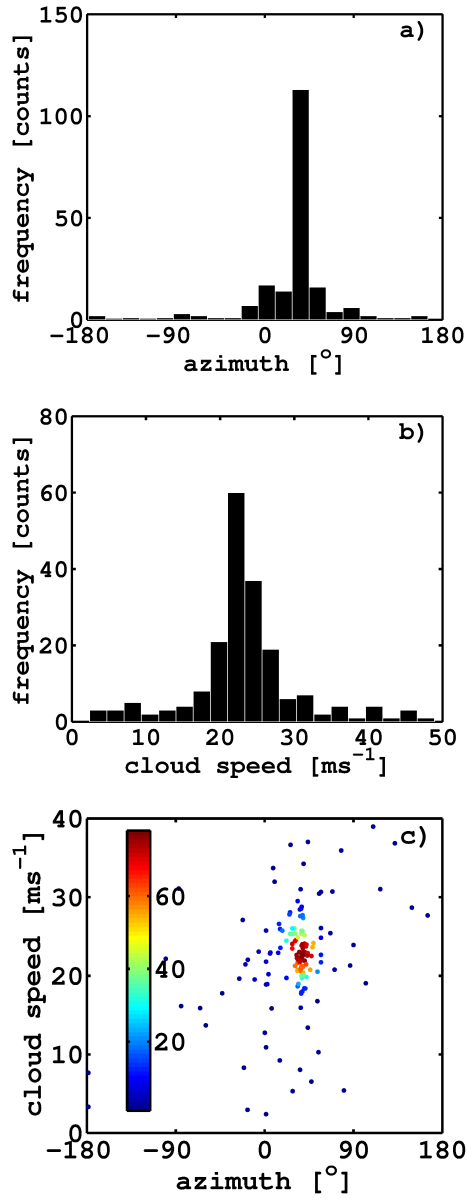


Figure 4: Distribution of the 192 pairs of cloud direction and speed obtained on October 24, 2011 between 1030-1130 PST. a) Histogram of the azimuths. b) Histogram of the cloud speeds. c) Scatter plot of the speed/azimuth pairs showing a density peak for the 21.9 ms<sup>-1</sup>/40.5° pair.

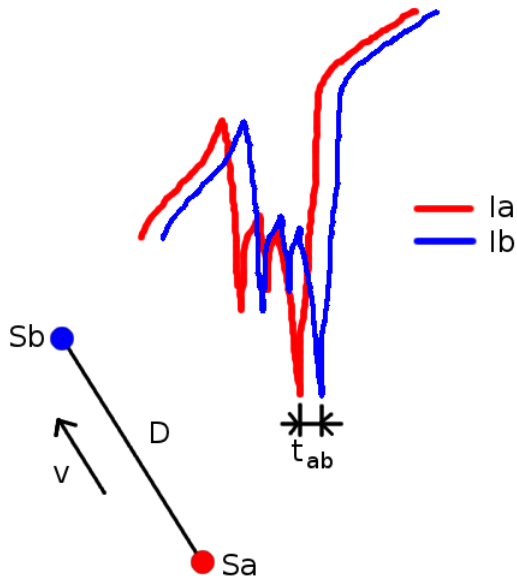


Figure 5: Sample sensor pair with spacing  $D$  aligned in the cloud motion direction and irradiance time series  $I_A$  and  $I_B$  (used with permission from Bosch et al. (2013)).

Previous results from a sensor array in a semi-circle with diameter 12 m Bosch et al. (2013) show that cross-correlation and linear cloud edge methods yield similar values for CMV direction, and this study will use the CCM as a validation for the LCE cloud speeds.

After quality control has been applied to the LCE results, the cloud direction is obtained from Fig. 4 and a pair of inverters aligned with the cloud direction is used to obtain the cloud speed.

The combinations in pairs of the 96 inverters cover the whole range of possible directions, but with different separation distances (Fig. 6). First, the most aligned pairs (within 1 degree of the cloud direction) are preselected from the initial set of 4560 pairs. From the most aligned pairs, the one with a separation distance closest to 500m is selected and used for the CCM cloud speed algorithm. For example, the inverters chosen for the period in Fig. 4 are marked in Figs. 1 (markers A and B) and 6. A 3 min time series is used to compute the cross-correlation. Finally, for quality control cloud speeds with a correlation coefficient between the power output time series of less than 0.78 are discarded. For example, the CMV results for 1130 PST October 24, 2011 were [ $v=21.9 \text{ ms}^{-1}$ ,  $\alpha=40.5^\circ$ ] for the LCE method and [ $v=22.7 \text{ ms}^{-1}$ ,  $R=0.799$ ] for the CCM method. The final number of CCM speeds that passed this last QC for October 24, 2011 was 37, which will be compared with the LCE speeds in the Results and Discussion section.

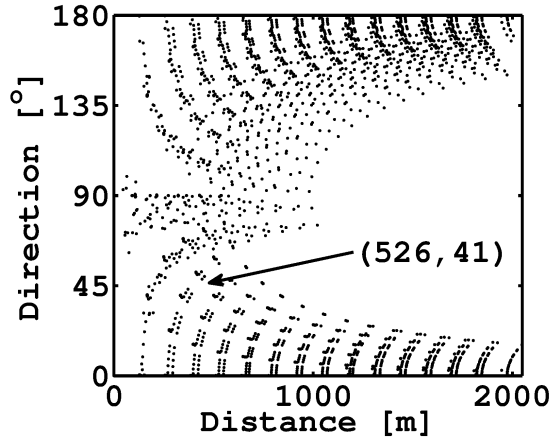


Figure 6: Distance and direction between all possible inverters combination. A direction of  $0^\circ$  indicates east.

#### 4. Results and Discussion

After discarding the completely clear days, the LCE method was used on the remaining 226 days to obtain pairs of cloud speed and direction using the quality control described in Section 3.2.2. Following the procedure in Section 3.3 the CCM method was applied and cloud speed was calculated independently. The year was split into four seasons to study the seasonal variation of the model performance. The periods considered are Q1 (January-March 2012, winter frontal systems), Q2 (April-June 2012, mostly clear), Q3 (July-September 2011, monsoon clouds) and Q4 (October-December 2011, winter frontal systems).

A total of 2700 cloud speeds from both the LCE ( $v_l$ ) and CCM ( $v_m$ ) methods were compared in terms of Root Mean Squared Error (RMSE) and Mean Bias Error (MBE) as defined by Eq. 16. The CCM cloud speed is considered as the ground truth and the errors are calculated as a percentage of the mean CCM speed value  $\bar{v}_m$ .

$$\begin{aligned}
 RMSE &= \sqrt{\frac{\sum_{i=1}^n (v_l(i) - v_m(i))^2}{n}} \frac{100}{\bar{v}_m} \% \\
 MBE &= \frac{\sum_{i=1}^n (v_l(i) - v_m(i))}{n} \frac{100}{\bar{v}_m} \%
 \end{aligned} \tag{16}$$

Figures 7 and 8 show the cloud speeds from the LCE and CCM methods and normalized power output from the inverters. It can be observed that CMVs are detected during the whole year except on clear days which mostly occurred in June, October and December. Some of the cloudy days do not contain any CMVs due to the quality control process. Also January and November show the largest intra-day variability in CMV. The general trend of the speeds detected by both methods follow the same yearly pattern, as corroborated by the errors obtained for the different quarters.

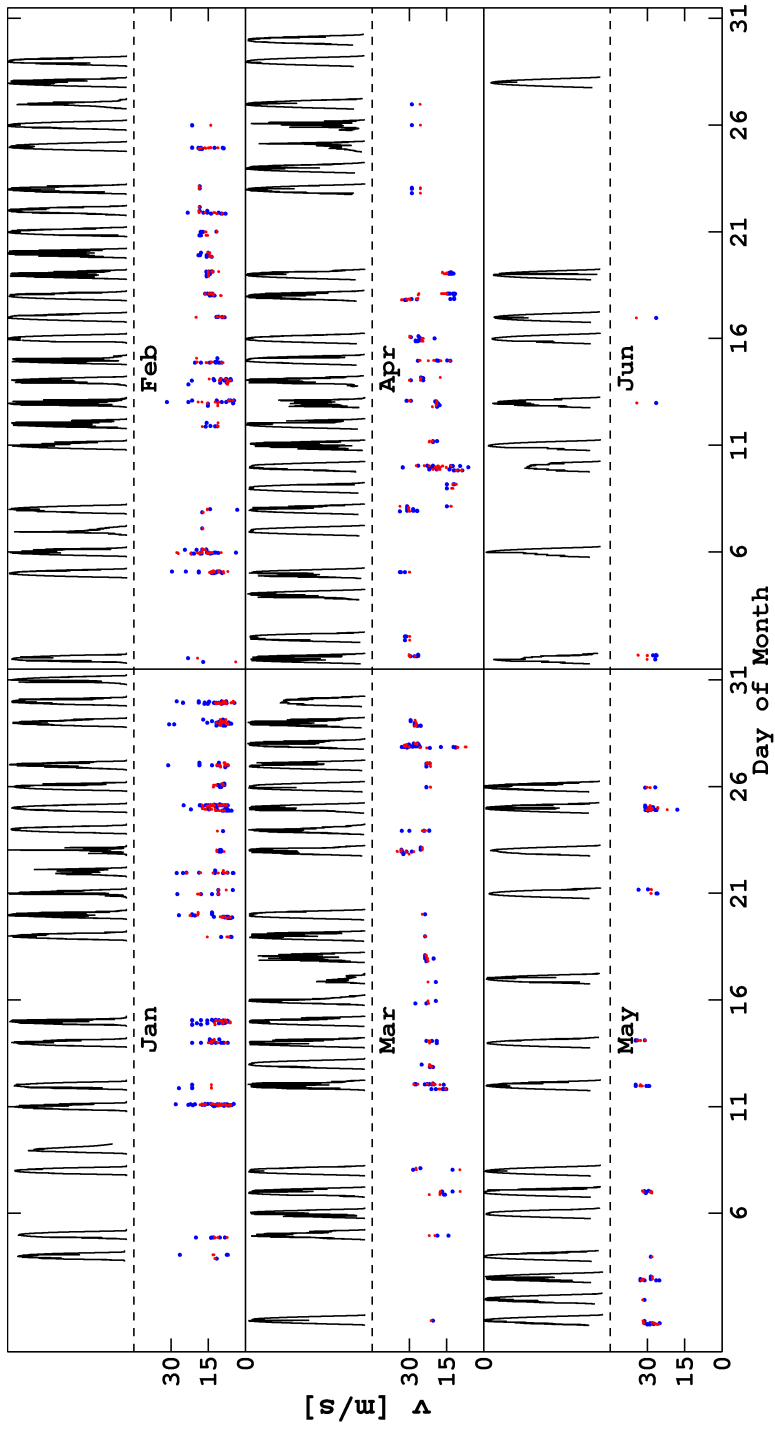


Figure 7: LCE (blue) and CCM (red) cloud speed from 0 to 35  $\text{ms}^{-1}$  for January-June 2012.

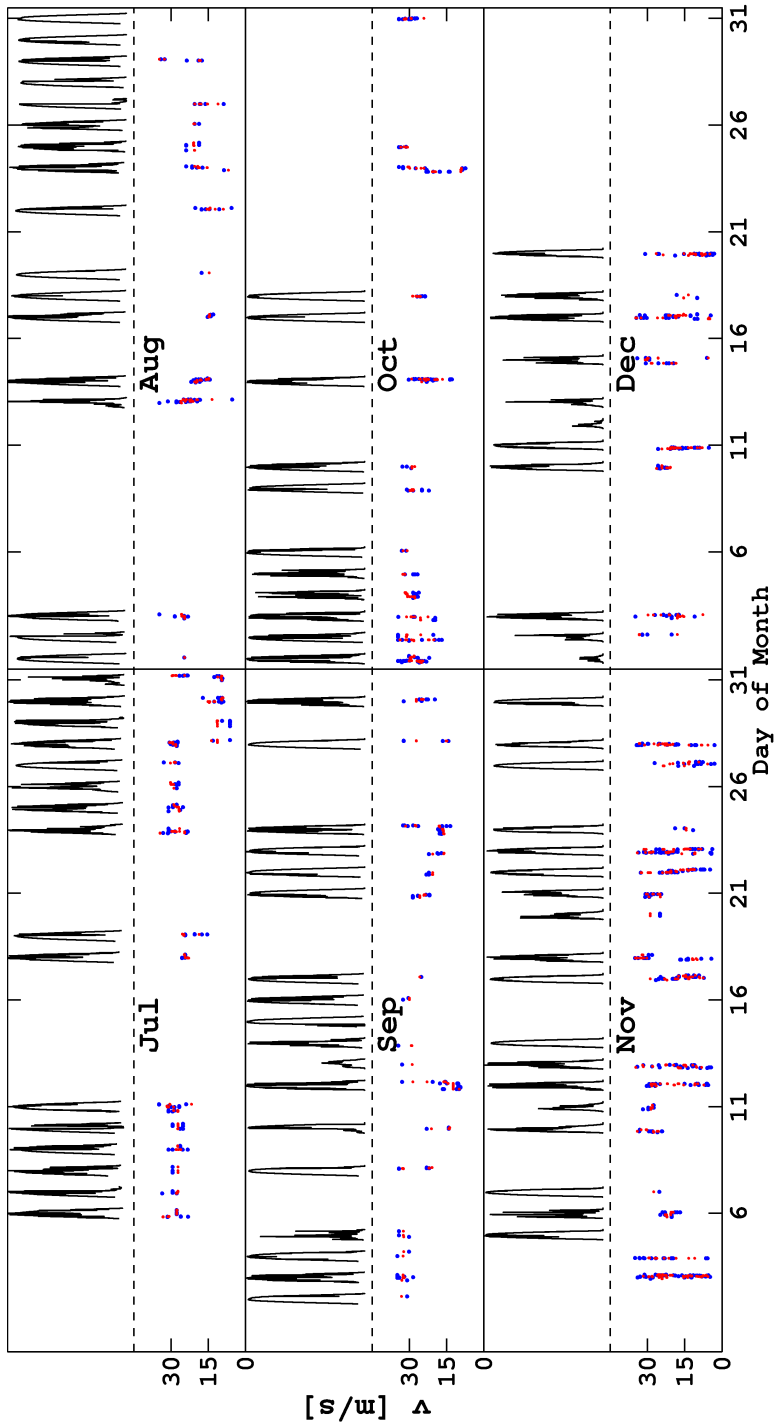


Figure 8: LCE (blue) and CCM (red) cloud speed from 0 to 35  $\text{ms}^{-1}$  for July-December 2011.

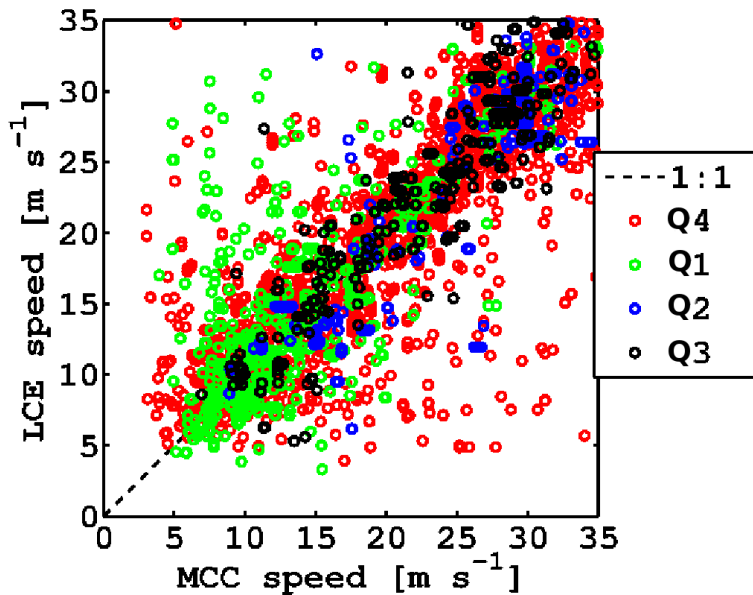


Figure 9: LCE vs CCM cloud speed for the whole year.

Fig. 9 shows the combined scatter plot of cloud speeds in the different seasons. The largest spreads are evident for the first and fourth terms, but with an overall grouping around the 1:1 line. It is worth noting that even though the CCM results are considered the ground truth, they have been calculated from the cloud direction detected by the LCE method. While cloud directions observed from both methods are generally very similar (Bosch et al. (2013)), this assumption will cause some of the spread observed in Fig. 9.

In addition, Table 2 show the validation of LCE results against the CCM separated by season. The average detected cloud speeds are lower for the first quarter of the year. The first quarter also registered the largest relative errors for both RMSE and MBE, showing a general trend of the LCE results to underestimate the CCM output. The second quarter shows the largest speeds and a relatively small RMSE and MBE. The third and fourth quarters show similar average cloud speeds and also a small MBE, with the overall smallest RMSE during the third quarter. The combined -0.9% MBE shows that both methodologies yield similar results even though they are based on very different concepts and data.

## 5. Conclusions

Irradiance and PV production data from a PV plant are used to estimate cloud speed which ranged from 3 to 35  $\text{m s}^{-1}$  over 1 year of data. Encouraging CMV results are obtained from the new LCE method applied to data from two triplets of reference cells with arbitrary orientations when compared to the more

Table 2: Error metrics for cloud speed by season including number of days and average speeds.

Period	Days	$v_{mean} \text{ms}^{-1}$	RMSE %	MBE %
Q1	66	15.0	29.3	-5.5
Q2	46	25.9	14.7	2.7
Q3	56	22.9	13.7	-1.2
Q4	58	22.5	21.8	0.7
All	226	21.6	20.9	-0.9

robust cross-correlation method. The results indicate that -especially if only a reduced number of sensors is available- LCE is a reliable option for cloud speed detection with an overall annual RMSE of 20.9%. A seasonal dependence of cloud speeds and the accuracy of detection was observed, with the best agreement between both methods during the July-September period yielding 13.7% RMSE and -1.2% MBE.

Future work will repeat this analysis in different areas to study the generality of the developed models, e.g. to confirm the performance for lower cloud speeds typical for coastal regions. The CMVs will also be applied to evaluate whether they enable more accurate forecast and variability models. A more comprehensive CMV database could be assembled which is currently lacking due to the inherent difficulty of cloud speed measurements.

## Acknowledgments

This work was supported by the California Solar Initiative RD&D program. We also appreciate the help of David Jeon, Leslie Padilla, and Shiva Bahuman from Sempra US Gas and Power and Bryan Urquhart from UCSD for providing and supporting the Copper Mountain data.

Arias Castro, E., Kleissl, J., Lave, M., 2013. A Poisson Model for Anisotropic Solar Ramp Rate Correlations. Submitted to Solar Energy.

Bosch, J., Zheng, Y., Kleissl, J., 2013. Deriving cloud velocity from an array of solar radiation measurements. Solar Energy 87, 196 – 203.

Chow, C.W., Urquhart, B., Lave, M., Dominguez, A., Kleissl, J., Shields, J., Washom, B., 2011. Intra-hour forecasting with a total sky imager at the UCSan Diego solar energy testbed. Solar Energy 85, 2881–2893.

First Solar, 2011. Copper Mountain Solar 1 datasheet. Available through: <http://www.firstsolar.com/Projects/Copper-Mountain-Solar-1> [Accessed 23 May 2013].

Google Earth 6.0, 2013. PV plant at Henderson (NV) 35°47'00.06"N, 114°59'33.10"W, elevation 564m. Available through: <http://www.google.com/earth/index.html> [Accessed 8 February 2013].

- Hammer, A., Heinemann, D., Lorenz, E., Lücke, B., 1999. Short-term forecasting of solar radiation: a statistical approach using satellite data. *Solar Energy* 67, 139–150.
- Hoff, T.E., Perez, R., 2010. Quantifying PV power output variability. *Solar Energy* 84, 1782–1793.
- Lave, M., Kleissl, J., 2013. Cloud speed impact on solar variability scaling - Application to the Wavelet Variability Model. *Solar Energy* , In Press.
- Leese, J.A., Novak, C.S., Clark, B.B., 1971. An automated technique for obtaining cloud motion from geosynchronous satellite data using cross correlation. *Journal of Applied Meteorology* 10, 118–132.
- Lorenz, E., Hammer, A., Heinemann, D., 2004. Short term forecasting of solar radiation based on satellite data. Proc. ISES Europe Solar Congress EURO-SUN2004, Freiburg, Germany, 2004 .
- Pelland, S., Galanis, G., Kallos, G., 2011. Solar and photovoltaic forecasting through post-processing of the Global Environmental Multiscale numerical weather prediction model. *Progress in Photovoltaics: Research and Applications* [Http://dx.doi.org/10.1002/pip.1180](http://dx.doi.org/10.1002/pip.1180).
- Perez, R., Kivalov, S., Schlemmer, J., Jr., K.H., Renné, D., Hoff, T.E., 2010. Validation of short and medium term operational solar radiation forecasts in the US. *Solar Energy* 84, 2161–2172.
- Yang, H., Chow, C.W., Ghonima, M., Kurtz, B., Nguyen, A., Urquhart, B., Kleissl, J., 2013. Solar irradiance forecasting using a ground-based sky imager developed at UC San Diego. Submitted to *Solar Energy*.